

Field tests for round-trip imaging at a 1.4 km distance with change detection and ranging using a short-wave infrared super-continuum laser

MOHAMMED N. ISLAM,^{1,2,*} MICHAEL J. FREEMAN,² LAUREN M. PETERSON,² KEVIN KE,² AGUSTIN IFARRAGUERRI,³ CHRISTOPHER BAILEY,⁴ FRANK BAXLEY,⁴ MICHAEL WAGER,⁴ ANTHONY ABSI,⁵ JAMES LEONARD,⁵ HYATT BAKER,⁵ AND MICHAEL RUCCI⁵

¹University of Michigan, Ann Arbor, Michigan 48109, USA

²Omni Sciences, Inc., Dexter, Michigan 48130, USA

³Leidos, Inc., Arlington, Virginia 22203, USA

⁴Leidos, Inc., Beavercreek, Ohio 45431, USA

⁵Air Force Research Laboratory, WPAFB, Ohio 45433, USA

*Corresponding author: mni@eecs.umich.edu

Received 13 November 2015; revised 11 January 2016; accepted 11 January 2016; posted 12 January 2016 (Doc. ID 253683); published 25 February 2016

Field tests have been conducted of a broadband illuminator for active hyperspectral imaging (HSI) using a short-wave infrared supercontinuum laser (SWIR-SCL). We demonstrated irradiance comparable to the sun for two-way measurements at a 1.4 km distance between laser and target, and performed change detection and ranging. The experimental results suggest that the range resolution of our method is ~ 1.5 cm even at the 1.4 km distance. Hence, we demonstrated the possibility to perform HSI with active broadband illumination using the SWIR-SCL. To our knowledge, this experiment is the first-ever to test two-way propagation of the active HSI illumination over a long distance. The 64 W SWIR-SCL provides near sunlight-equivalent illumination over multiple square meters, and the laser could enable HSI 24 h a day, even under a cloud cover, as well as enhanced capabilities such as change detection and ranging. © 2016 Optical Society of America

OCIS codes: (110.3080) Infrared imaging; (060.2320) Fiber optics amplifiers and oscillators; (140.3070) Infrared and far-infrared lasers; (280.0280) Remote sensing and sensors; (320.6629) Supercontinuum generation.

<http://dx.doi.org/10.1364/AO.55.001584>

1. INTRODUCTION

We have conducted field trials showing the feasibility of using a high-power, short-wave infrared (SWIR) supercontinuum laser (SCL) as an active illuminator for hyperspectral imaging (HSI). The SWIR-SCL with light intensity comparable to the sun was used in field trials at Wright-Patterson Air Force Base (WPAFB, Air Force Research Laboratory, Dayton, Ohio), where the laser was placed in a 12-story tower and the targets were placed on the ground at a distance of 1.4 km or more. The SWIR-SCL delivered 64 W time-averaged output power over the continuous wavelength range from 1064 to >1800 nm with a wall-plug efficiency of 15.7% and a beam quality that is nearly diffraction-limited with $M^2 < 1.3$ over the wavelength range. Also, the SWIR-SCL produces ~ 0.45 ns pulses with a repetition rate near 6.25 MHz and an average relative variability or fluctuation of $\pm 0.2\%$. This SWIR-SCL along

with various diagnostics including a hyperspectral imaging camera were placed in the 12-story tower, while targets on an $8' \times 8'$ plywood board were placed on the ground, normal to the beam, at a distance of 1.4 km or more.

The field tests demonstrated three significant outcomes. First, because of the high brightness from the SWIR-SCL, the diffuse reflection from targets at a distance of 1.4 km could be detected by the hyperspectral imaging camera placed adjacent to the laser. In particular, we demonstrated end-to-end stand-off sensing with a SWIR hyperspectral camera at a distance of 1.4 km on a slant path near the ground. Second, the SWIR-SCL was successfully used for a broadband change detection demonstration experiment, where the laser was on-off modulated at 15 Hz synchronized to the 30 Hz frame rate of an observing SWIR camera and receiver telescope. In the change detection process, camera frames with laser off are subtracted from the

frames with laser on, thereby cancelling or minimizing artifacts associated with the sun illumination, the change in angle of the sun, and shadows. Third, similar to LIDAR techniques, ranging was used to measure the distance of the target with an absolute accuracy of ~ 1.5 cm even at distances of 1.4 km or more.

The ranging measured the ~ 0.45 ns pulses from the SWIR-SCL using a time-of-flight and modulated laser technique. These field test results confirm the feasibility of using the SWIR-SCL as an active illuminator for hyperspectral imaging, thereby permitting 24/7 operation and in shadowed conditions, rather than being restricted to sun-light operation. Moreover, beyond simply providing sun-equivalent illumination, the SWIR-SCL also permits broadband change detection and ranging, which are not possible with passive hyperspectral imaging using the sun.

2. MOTIVATION AND BACKGROUND

Supercontinuum lasers blend the desirable attributes of a laser and a lamp [1]. Similar to many lasers, the SCL produces a spatially coherent, nearly diffraction-limited beam with high brightness that can propagate for long distances with minimum divergence. On the other hand, lasers tend to be very spectrally narrowband. In contrast, the SCL produces, similar to a lamp, a broad continuous spectrum that can cover several octaves of light. In this paper, we investigated the use of SCL technology to provide active illumination for SWIR hyperspectral sensors to extend their operational window into the night and heavy overcast periods.

Passive hyperspectral imaging systems that are illuminated by sunlight have a number of limitations that we aim to overcome using the SCL technology. Useful HSI data requires sun angles available for no more than seven hours each clear day, depending on the location and time of year. Cloud cover also reduces illumination and restricts the utility of the HSI data. Moving beyond these limitations requires active illumination, which can extend the operational envelope of the technology to 24 h. Additional advantages of active illumination include the elimination of shadows (when the source and receiver are co-located) that alter the measured spectral signature and increase false alarms, improved change detection by providing a consistent illumination geometry, direct retrieval of surface reflectance at short ranges, and with modulated sources the possibility of ranging and forest canopy penetration.

There are two possibilities to illuminate a surface for spectral interrogation: lamps and lasers. Lamps can produce smooth, broadband illumination that can be customized by optical filtering, but to maintain brightness at multikilometer ranges the beam must be highly collimated and spatially coherent, neither of which have been efficiently achieved with lamps thus far. Lasers, on the other hand, have the correct spatial characteristics to deliver high brightness at a distance, but have been limited in wavelength range.

Previous attempts at active HSI illumination have focused on laser sources at selected wavelengths, but this approach gives up a great deal on information at wavelengths that are not illuminated. In the late 1990s, researchers at MIT's Lincoln Laboratory built two prototype imaging spectrometers using "white light" lasers that took advantage of the stimulated Raman scattering effect [2,3]. However, they were not able

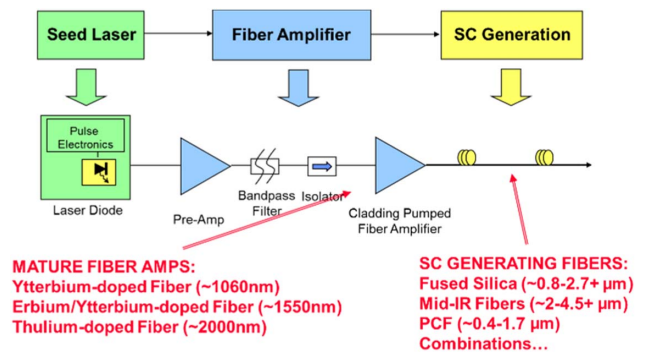


Fig. 1. Top-level SC generation design using all-COTS components.

to move beyond the laboratory due to the low available laser output power. More recently, a 25-band laser detection and ranging system was demonstrated that is capable of up to 40 m range [4]. With the rapid advances in high-power diode laser pumps, it has now become possible to develop a broadband laser illuminator based on SCL technology with sufficient intensity at range to match the sunlight [5,6]. Our development efforts have concentrated in the SWIR region of the spectrum, but this technology is also applicable in the visible and in the mid-wave infrared.

Supercontinuum (SC) lasers are the first technology to successfully combine spectrally broadband characteristics with laser spatial performance. To create a supercontinuum output in a spatially coherent laser, a diode laser output is optically amplified and used to pump a short length of highly nonlinear optical fiber (Fig. 1). Use of modulation instability and stimulated Raman scattering in the fiber enables the use of compact laser diodes as the primary source of energy while maintaining spatial coherence [9]. SC generation has been demonstrated at wavelengths as short as $0.35\text{ }\mu\text{m}$ and as long as $4.5\text{ }\mu\text{m}$, and extension to $5.5\text{ }\mu\text{m}$ is possible with new indium fluoride fibers [7,8–10].

A. SWIR Super-Continuum Generation Techniques

SC lasers in the IR have been demonstrated in various pump and fiber configurations. Two approaches to generate SC are widely used: pumping a short length of nonlinear fiber using femtosecond pulses with high peak power or using continuous wave (CW)/quasi-CW with lower peak power to pump longer lengths of fiber. For example, a mode-locked femtosecond erbium fiber laser was used to generate SC ranging from 0.8 to $2.7\text{ }\mu\text{m}$ in just 12 cm of highly nonlinear silica fiber [11]. Moon and Kim, reported an SC extending from ~ 0.8 to $1.7\text{ }\mu\text{m}$ in dispersion-shifted fiber using amplified laser diode pulses with 30 ps pulse width [12]. In contrast, Xia *et al.*, reported a $\sim 5.3\text{ W}$ SC ranging from $\sim 0.8\text{-}3\text{ }\mu\text{m}$ in highly nonlinear silica fiber using nanosecond diode pulses amplified with a multi-stage amplifier [9,10]. In the CW regime, Abeeluck and Headly, reported an SC generation extending beyond $1.75\text{ }\mu\text{m}$ and $\sim 5\text{ W}$ average output power in 500 m of highly nonlinear fibers pumped using a CW Raman fiber laser [13]. Pumps based on ytterbium-doped fiber amplifiers (YDFA) have also been used to demonstrate high-power SC generation in silica-based photonic crystal fibers. For example, time

average powers of ~ 29 W in an SC extending from 1.06 to 1.67 μm using a CW ytterbium fiber laser has been demonstrated [14]. Time average powers of ~ 39 W in an SC extending from 0.4 to 2.25 μm using a picosecond YDFA MOPA pump source have also been reported [15]. Since then, the pump wavelength has been limited to $\sim 1\text{--}1.2$ μm for YDFA-based pumps; the SC in this case extends out only to ~ 2.25 μm on the long wavelength side.

Our group also has built and field tested other SC lasers for active remote sensing and hyperspectral imaging. For example, a 5 W SWIR SC Laser operating from 1550 to 2300 nm was built and field-tested at WPAFB by Air Force Research Labs [6]. We showed that the nearly diffraction-limited beam propagated from a 12-story tower to targets a mile away, and we were able to identify different targets using hyperspectral measurements. However, the diffuse-reflected signal could not reach back to the tower at this power level (the current paper describes the higher power level where the signal can be detected back at the tower). In addition, we demonstrated and characterized in the laboratory a 25 W SC laser generating light from approximately 1900 to 2400 nm based on a thulium power amplifier [5]. As described further in this paper, the 25 W SC output provides light at a comparable or higher intensity than solar illumination in the lasers wavelength range, and demonstrates that practical high-power supercontinuum generation is possible across the entire SWIR range from 1 to 2.4 μm .

3. HIGH-POWER SWIR SUPER-CONTINUUM LASER PROTOTYPE

Figure 2(a) shows a block diagram of our SWIR SCL. Also, Fig. 2(b) presents a photograph of the SWIR-SCL prototype.

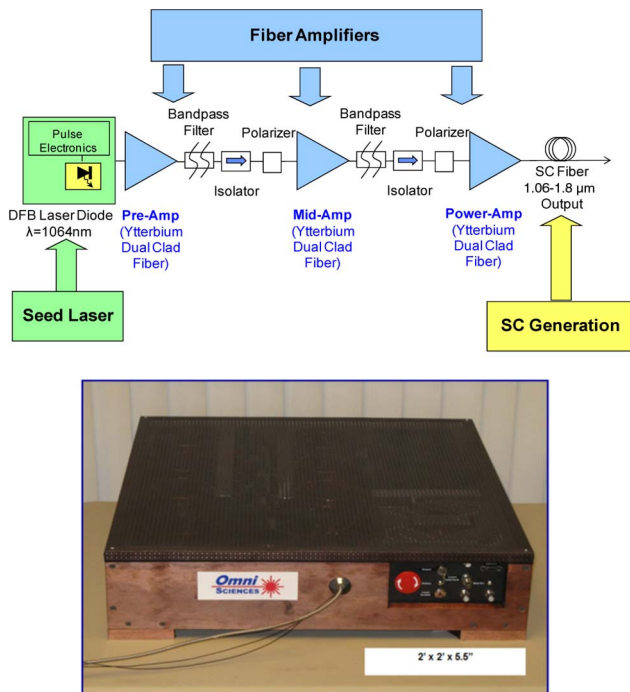


Fig. 2. (a) Laser configuration for the 64 W SWIR supercontinuum laser. (b) Photograph of the SWIR-SCL prototype used in the field-test experiments.

The configuration is a master oscillator power amplifier with a 0.45 ns pulsed DFB laser diode at 1064 nm as the seed oscillator. Amplification of the 1064 nm radiation is achieved with three YDFA stages each with their own high power 915 nm pump laser diodes that provide fiber cladding pumping. The first stage pre-amplifier is designed for optimal noise performance. Between amplifier stages, bandpass filters and polarizers block amplified spontaneous emission (ASE) and isolators suppress spurious reflections and backward propagating ASE. The power amplifier stage is optimized to minimize nonlinear distortion. This pump-laser configuration is a common and standard telecom design [7,1].

The high average power of our SC laser was achieved with three separate amplifier stages, as shown in Fig. 2. Each amplifier is double-clad (dual-core) polarization-maintaining fiber with 1064 nm radiation propagating in the Yb-doped core and CW 915 nm pump radiation propagating in the cladding. The pre-amp stage delivers ~ 28 dB of gain, the mid-stage ~ 28 dB of gain, and the power-amp stage ~ 23 dB of gain, while the between stage components exhibit ~ 4 dB of loss. The output from the power amplifier is a train of ~ 0.45 ns pulses with peak power of about 24 KW. These intense pulses are coupled to the SC generation fiber.

The spectral broadening for the SC laser occurs in the undoped fiber that follows the power amplifier. The SC generation fiber is approximately 10 m long, has a core diameter of 25 μm , and has a 0.065 numerical aperture. Figure 3 shows the SWIR-SCL output spectral power from 800 to 2200 nm measured with our Acton 2150i 0.15 meter scanning monochromator and a TE-cooled HgCdTe (5.2 μm cut-off wavelength) detector. The raw spectrum was corrected for the approximately linear spectral response of the detector. Figure 3(a) shows the spectral output on a logarithmic scale, while Fig. 3(b) shows the spectral output on a linear scale.

The features exhibited in the SWIR-SCL spectrum may be explained as follows. Since the ~ 1064 nm pump wavelength is

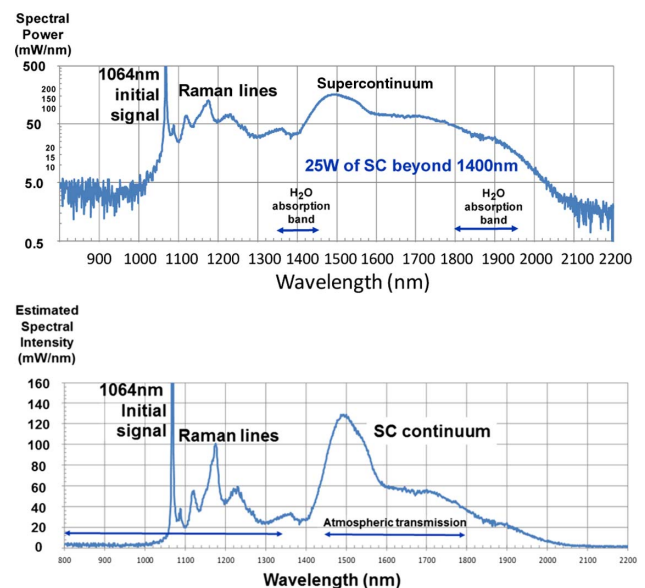


Fig. 3. 64 W average SWIR-SCL spectral output at 6.25 MHz repetition rate plotted on (a) logarithmic and (b) linear scale.

well below the zero dispersion wavelength of the fiber (near 1300 nm), the dominant nonlinear mechanism for the ~ 0.45 ns long pulses in the fiber is stimulated Raman scattering at the pump wavelength [1,16]. For fused silica fiber as used in the SC generation here, the peak Raman gain is about 440 cm^{-1} or ~ 13.2 THz lower energy (or longer wavelength) compared to the pump. Therefore, the peaks observed in the spectrum between roughly 1064 and 1300 nm correspond to different cascaded Raman frequency-shifted orders [16]. Once the cascaded Raman shifting process downshifts significant energy to wavelengths longer than ~ 1300 nm, the Raman shifted light is in the anomalous group-velocity dispersion regime—often called the soliton regime. For high peak powers in the soliton regime, the sub-nanosecond pulses are unstable due to a phenomenon known as modulational instability, which is parametric amplification in which the fiber nonlinearity helps to phase match the pulses. In particular, modulational instability tries to form soliton pulses from the quasi-continuous-wave background of the sub-nanosecond pulses, so that the sub-nanosecond pulses are broken into numerous picosecond pulses with higher peak intensity [8,17].

The short pulses created through modulation instability then propagate through the SC fiber to generate the broadband continuum. The nonlinear mechanisms leading to broadband SC include four-wave mixing and self-phase modulation to generate a cascading of sidebands. For sufficient peak power and SC fiber length, the SC generation process fills the long-wavelength spectrum up to the transmission window limit of the fiber. Hence, the spectrum from ~ 1300 nm to ~ 2200 nm in Fig. 2 corresponds to the smoother, continuous SC generated light.

Measurements were made to demonstrate the progression of the supercontinuum process with pump power. For these measurements, the diode laser pump power to the power amplifier was increased linearly from 8 to 165 W while maintaining a fixed repetition rate of 6.25 MHz. As the pump power increased, the peak power from the power amplifier also increased. This leads to a greater proliferation of nonlinear effects in the SC fiber, which leads to laser broadening to longer wavelengths. Figure 4 presents the results, where spectral output is displayed for various pump powers. The powers listed in the box are the increasing total laser output powers for

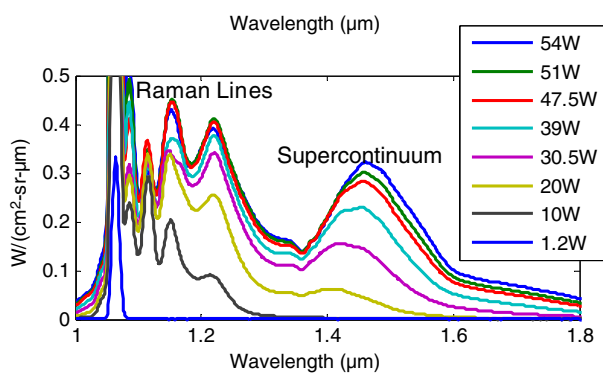


Fig. 4. Spectral reflected radiance and total output power of our SWIR-SC laser as diode laser pumping is increased for a fixed repetition rate of 6.25 MHz.

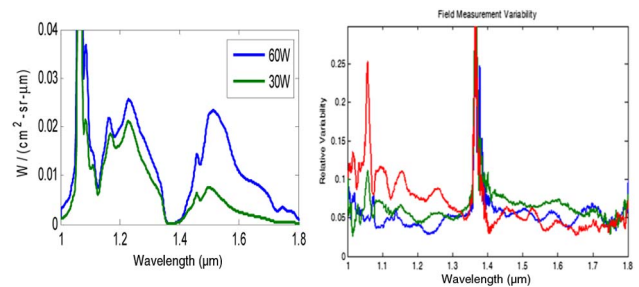


Fig. 5. Nighttime SC laser radiance from a white Tyvek target at 1.4 km range (left) and field measurement of the variability, which is primarily from atmospheric turbulence.

the increasing diode laser pump powers. As the pump power is increased, we first observed the wavelengths corresponding to the cascaded Raman process. Then, as significant power shifts beyond ~ 1300 nm, the SC generation process takes over to shift energy beyond the zero dispersion wavelength out to 1800 nm and longer. There is still considerable residual pump power near ~ 1064 nm, which we believe can be better depleted by increasing the peak power and further optimizing the SC generation fiber type and length. For these experiments, we did not try to expand the wavelength much beyond 1800 nm, since the atmospheric absorption would attenuate the light in the field.

To illustrate the effect of the atmospheric absorption on the spectrum, we also measured the spectrum after propagation through the atmosphere in the field tests. For example, Fig. 5 illustrates the nighttime spectral radiance from a highly reflecting white Tyvek target illuminated with our SWIR-SC laser and measured with a field spectrometer operating from 1000 to 2000 nm. The laser path is nearly horizontal (3.1 deg depression angle) over a distance of 1.4 km from a 76 m high 12-story tower to the ground (further discussed in next section and Fig. 9). Water-vapor absorption is evident around 1.4 and 1.8 μm . Although the laboratory measurements of the laser output showed variability of only 0.04% RMS (Fig. 7), the variability of the radiance signal in the field was 5.8% RMS due primarily to atmospheric turbulence, as shown on the right side of Fig. 5 [4,8].

It is possible to vary the time-averaged power for the SWIR-SC by varying the repetition rate of the seed laser pulses [5]. As the repetition rate is increased, the output power increases approximately linearly and a nearly constant spectrum can be obtained if the parameters are adjusted to maintain a nearly constant peak power (e.g., peak power determines the spectrum, while repetition rate determines the time averaged power). For example, Fig. 6 plots the output SC power versus repetition rate, as the repetition rate is varied between 1 and 7 MHz. For each of these data points the power amplifier pump level was adjusted to obtain a peak power of approximately 24 kW, which is the peak power from the power amplifier going into the SC fiber.

We also characterized the amplitude stability of the output from the SWIR-SCL light source. The quasi-continuous power output of our 64 W SWIR-SCL was measured over a period of 15 h and was found to have excellent amplitude stability.

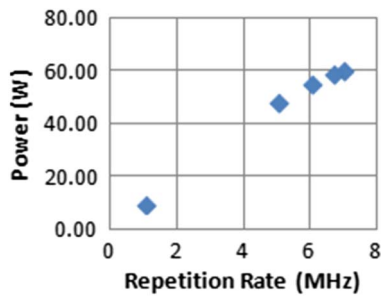


Fig. 6. Output SWIR-SCL power versus repetition rate of the seed laser.

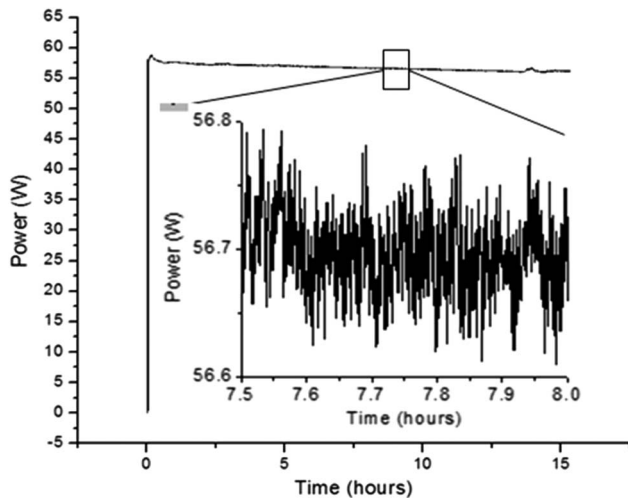


Fig. 7. SWIR-SCL output power stability versus time. Insert shows a blow-up of the power in the time window indicated by the box.

Figure 7 shows average laser output power as a function of time over the long measurement. After the SWIR-SCL warmed up for a time on the order of 20 min (e.g., all the optics in the box reached a steady-state temperature), the output power remained quite stable. The box in the figure shows an expanded power and time scale to show details of the amplitude fluctuations. In particular, the power fluctuation was measured to be $\pm 0.2\%$ peak-to-peak, or 0.04% RMS.

The wall-plug efficiency of the 64 W SWIR-SCL was also measured in the laboratory. The power drawn from the standard wall plug was measured using a “Kill-A-Watt” electricity monitor. We define the wall-plug efficiency as the output power from the SWIR-SCL as measured by a time-averaging power meter divided by the power drawn from the standard wall plug. It is important to note that this metric includes the electrical power supply, all of the electronics, the optical-to-electrical efficiency of the pump lasers as well as the pump light to SC generation conversion efficiency. At full power operation with 64 W measured from the SC output, we measured a wall-plug efficiency of 15.7%. Such a high wall-plug efficiency is important for any application where the power has to be provided from an onboard system (e.g., aircraft or drone),

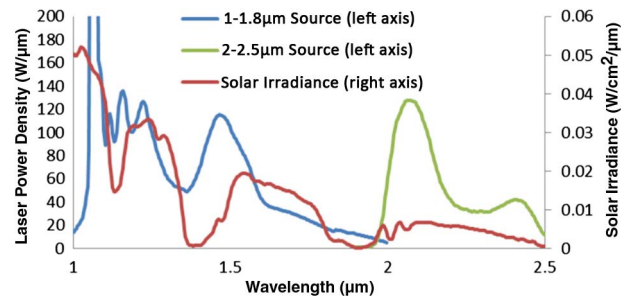


Fig. 8. Supercontinuum laser power density spectra from 1 to 1.8 μm source in this paper (blue curve), and 2–2.5 μm source from 25 W laboratory SC unit (green curve) [5]. Red curve corresponds to the solar irradiance spectrum over the SWIR wavelength range.

and the high efficiency also means that the heat generated from power dissipation will be minimized.

Initial calculations showed that to match sunlight, it would be necessary to generate at least between 50 and 100 $\text{W}/\mu\text{m}/\text{m}^2$, so we set a goal of SC output power density of 100 $\text{W}/\mu\text{m}$ as the initial benchmark [18]. Figure 8 plots the output power density spectra of the SWIR-SC of this paper (from 1.06 to 1.8 μm) as compared to solar irradiance at a 50° elevation (40° zenith angle). In 2012 we also built and tested a Thulium-based SC laboratory prototype in the 2–2.5 μm region with 25 W of SC output, or 50 $\text{W}/\mu\text{m}$ [5]. In the wavelength range of 2–2.5 μm , Fig. 8 shows the power density spectrum produced by the 25 W breadboard. Both power spectral densities were measured against a Spectralon target at approximately 1 m from the source. Thus, over a significant fraction of the wavelength range covered by the 64 W SWIR-SC of this paper, the output power density is comparable to or exceeds the solar spectrum when projected over a 1 m^2 area.

In summary, the SWIR-SCL prototype of Fig. 2 generates 64 W output over the wavelength range of 1064 to greater than 1800 nm. The output power fluctuation is measured to be $\pm 0.2\%$ peak-to-peak or 0.04% RMS, and the wall-plug efficiency is measured to be 15.7% at a 64 W output. Some of the advantages of the SC architecture of Figs. 1 and 2 include:

- All-fiber integrated, no moving parts. In other words, the laser has the potential to be compact and robust, with high reliability and a low maintenance cost.
- Leverage mature fiber optics and telecommunications technologies. All of the parts used in the laser are commercial off-the-shelf (COTS) components, which means that the price will continue to decrease and the performance will continue to increase due to a large market requiring the components.
- Simple, cost-effective design. The designs of Figs. 1 and 2 do not use mode-locked lasers, which helps keep the parts cost relatively low. Also, the cost-of-assembly can also be potentially low, since all the parts are fiber-based and can be spliced together with commercially available splicers.
- Platform for SC over the SWIR, mid-wave infrared, and visible. Although the focus of this paper is in the SWIR, different amplifiers (e.g., erbium, erbium/ytterbium, ytterbium, and thulium) and different fibers can be used to generate SC in other wavelength ranges [7,1].

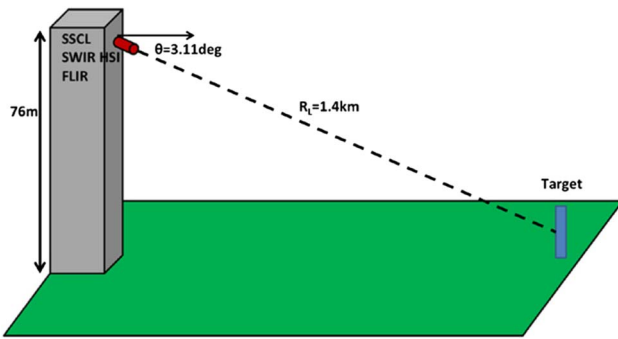


Fig. 9. Side view diagram of tower-based field test layout.

4. TESTING OF SWIR-SCL

The performance of the 64 W SWIR-SCL as a source for a bi-static active HSI sensor was evaluated at the Air Force Research Laboratory (AFRL) laser test facility located on WPAFB. We assessed the beam propagation characteristics of the laser and demonstrated reflectance retrieval. In the first tests, the majority of testing occurred after sunset to remove any solar contribution to the measured signal (next section will discuss change detection results, which were collected throughout the day). The SWIR-SCL was placed in a tower laboratory and directed along a slant path to a target panel on the ground. This target panel serves to provide a uniform background and as a backdrop for placement/holding of the target materials used during the collection. Figure 9 provides a side view diagram of the tower-based test setup. The materials used on the target panel include Tyvek, black silt cloth, gray silt cloth, a blue tarp, and gray-painted plywood. The stand is tilted slightly from vertical to create a normal surface with respect to the laser beam propagation angle (3.11 deg). In this diagram, we determined the laser range by the slant range from the tower (1.4 km). A broadband SWIR camera made by FLIR with spectral response from 1 to 5 μm was used to provide beam shape and turbulence analysis. Additionally, a slit-based SWIR hyperspectral imaging camera made by Headwall Photonics was used to measure the characteristics of the laser return signal as a function of wavelength. Both the broadband and HSI cameras were equipped with 100 mm lenses to provide multiple pixels across the 0.9 m laser spot diameter at a 1.4 km slant range. Table 1 provides other relevant laser and camera specifications for the tower test. Note that due to losses in the mirrors used to direct the laser beam from the tower, the effective laser power is approximately 55 W rather than the lab measured 64 W [19].

For a remote laser source, it is necessary to have limited divergence from the raw fiber output. We chose to use a

Table 1. Relevant Specifications for Tower Test

R_L (km)	1.4
Output power (W)	55
Full-angle at 1.4 μm (mrad)	0.636
Spot size at 1.4 μm (m)	0.9
I FOV (mrad)	0.3
GSD (cm)	42



Fig. 10. 64 W SWIR-SCL with fiber optic cable extending to the optical collimator.

gold-coated $f = 4$ inches off-axis parabolic mirror to collimate the laser radiation to a beam diameter of 8.8 mm ($1/e^2$) at the mirror. By doing so the divergence of our laser beam was reduced to a nearly diffraction-limited 0.24 mrad and a Rayleigh range of 44 m (see next section for further discussion of beam divergence). Greater divergences can be achieved by slightly moving (detuning) the position of the parabolic mirror. Figure 10 shows our laser in the laboratory with its fiber delivery cable to the optical collimator. Note that although the collimated laser beam divergence is 0.24 mrad, the measured divergence of the beam to the target is 0.635 mrad due to atmospheric turbulence (see Table 1).

A. Short-Range Characterization of Laser

We also measured the divergence of the laser beam emanating from the output fiber end from the SWIR-SCL and compared it to a diffraction-limited calculation to determine the M^2 value. We measured the far field diameter of the laser beam projected on a 12" Spectralon target at 3.0 m from the uncollimated fiber output using the FLIR camera. The measured $1/e^2$ diameter was approximately 259 mm, so that the bare fiber beam divergence is 86.3 mrad ($=5.0$ deg). Since the output fiber has a numerical aperture of ~ 0.065 and a 25 μm diameter core, we calculated a mode field diameter of 22.1 μm at the central wavelength of 1400 nm and 20.1 μm at 1064 nm. Using this mode field diameter, the calculated diffraction-limited $1/e^2$ beam divergence is 80.5 mrad at 1400 nm and 67.3 mrad at 1064 nm. The ratio of the measured beam divergence and the theoretical diffraction limited divergence gave us an $M^2 = 1.07$ at 1400 nm and 1.28 at 1064 nm. For the spread of wavelengths of our SC laser, we concluded a conservative $M^2 < 1.3$ over the full wavelength range.

We used the hyperspectral camera to collect spectral radiance data along a vertical line down the center portion of the beam. Figure 11 shows the results, including the average radiance spectrum compared to the temporal variability and the sensor's dark noise, and the beam profile for a subset of spectral bands across the spectral range of the laser. The beam profile is not perfectly Gaussian, which may be due to imperfect

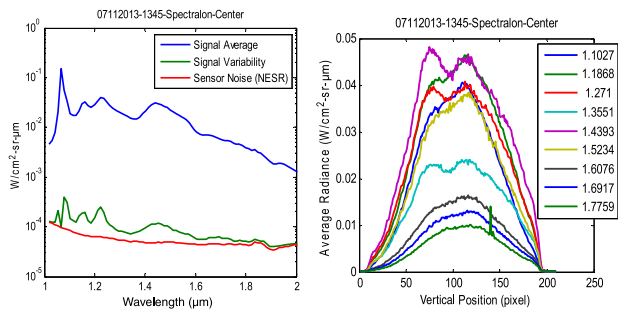


Fig. 11. Spatial-spectral characterization of the SWIR-SC beam profile in the lab. Graph (a) shows the average radiance spectrum compared to the temporal standard deviation and the sensor dark noise; (b) contains the vertical beam profiles at multiple wavelengths.

optics used to direct the beam as well as the angle cleave and the fiber cap.

B. Long-Range Characterization of Laser

The SWIR-SCL light was directed from the tower laboratory through seven relay mirrors to the 8' × 8' Tyvek target. Because the beam is less than a meter across at the 1.4 km distance, and the camera is looking at the image from 1.4 km away, only a few pixels show the beam spot. Figure 12 shows the spatial characterization. The FLIR camera was placed next to the SWIR-SCL source in the tower, and the image was taken using a 100 mm lens. The beam directing optics were cleaned and adjusted to minimize astigmatism due to heating of the mirror surfaces, although some distortion is clearly visible in the images. The images of Fig. 12 represent an average of 5000 samples taken at a 100 Hz frame rate. As shown on the right side of Fig. 12, the disk-equivalent diameters measured are 61 cm at 50% light intensity and 97 cm at 1/e² intensity.

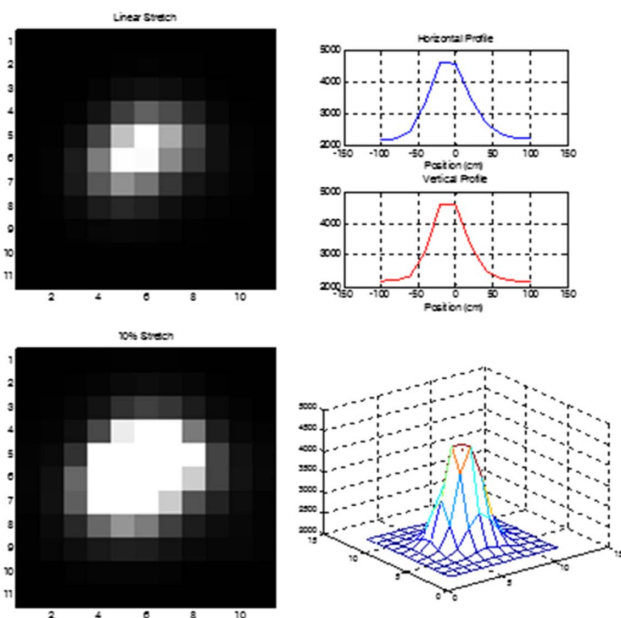


Fig. 12. Images taken with FLIR camera placed next to SWIR-SCL in tower. Image is of the illumination of the target 1.4 km, as seen from the diffuse reflected light.

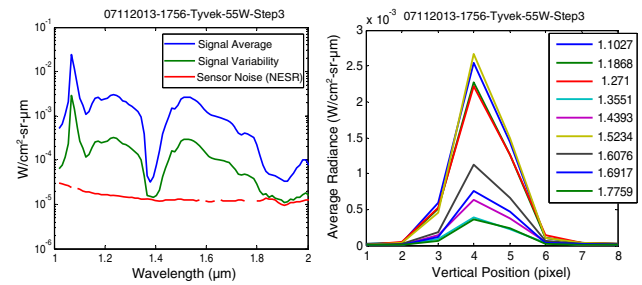


Fig. 13. Spatial-spectral characterization of the SWIR-SC beam profile for 1.4 km round trip. Graph (a) shows the average radiance spectrum compared to the temporal standard deviation and the sensor dark noise; (b) contains the vertical beam profiles at multiple wavelengths.

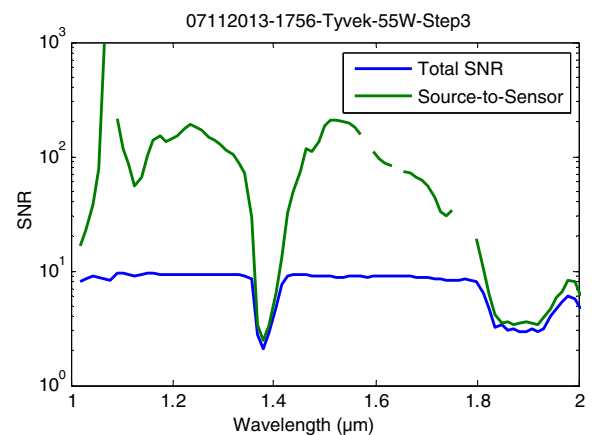


Fig. 14. Signal-to-noise ratios for the average return signal reflected from a Tyvek target versus the sensor dark noise (green curve) and the total variability including turbulence (blue curve).

Figure 13 shows the spatial-spectral characterization analogous to Fig. 11, but collected after 2-way propagation of the collimated beam over 1.4 km. The atmospheric spectral effects are clearly visible in the spectral radiance measurements (particularly the water absorption band at 1.4 μm). The measured signal variability is much greater than in the lab due to the strong effects of turbulence in the test geometry. The effects of turbulence are further quantified in Fig. 14, where we show that the ratio of the average return signal to the sensor noise is ~20 dB on average, but the ratio of the same signal to the total variability is only ~10 dB and generally spectrally constant since the turbulence noise is proportional to the signal. This result shows that at the 64 W power level there is adequate energy to measure the returning light from a beam propagated 1.4 km to the target where the beam is diffusely reflected.

C. Target Reflectance Estimation

Six materials were used as targets: Tyvek, gray-painted wood, black silt cloth, grass (by pointing the source off to the side of the target), gray silt cloth over Tyvek, and a blue plastic tarp. The Tyvek, black cloth, and blue tarp are all made primarily of

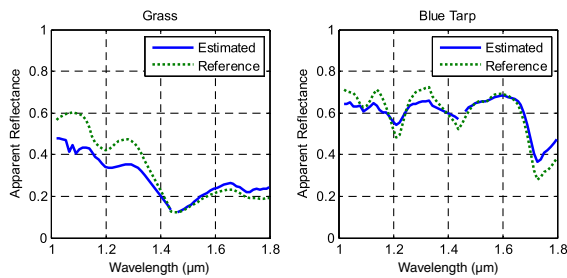


Fig. 15. Estimated apparent reflectance of the grass and blue tarp targets compared to the reference spectra. The target materials were placed 1.4 km away from the SWIR-SCL.

polyethylene. The gray silt cloth is made of polypropylene, which is spectrally similar to the polyethylene in the spectral region of the measurement. These materials were chosen to span the range of reflectance from $\sim 4\%$ (black cloth) to $\sim 90\%$ (Tyvek).

We compare the estimated apparent reflectance spectra of these materials against reference measurements. Since we did not have a reflectance standard such as Spectralon to provide a reference, we used the empirical line method (ELM) [20] to estimate the illumination and atmospheric parameters needed to convert the measured radiance to apparent reflectance. The brightest radiance spectrum was extracted from each image. The ELM parameters were computed by linear regression using all except the Tyvek spectrum, because inclusion of this measurement caused the results to be distorted and the spectral features were significantly diminished. This is likely due to the large specular component of the material, which is not captured by the reference measurements. The specular component is significant in the monostatic configuration that was used. Figure 15 shows the results for the grass and the blue tarp compared to the reference spectra of the materials. The spectral shapes match very well, with some noise caused by the sharp radiance spike from the pump residual at $1.06 \mu\text{m}$.

In summary for this section, the 64 W SWIR-SCL was field tested at WPAFB, where the laser was placed in a 12th floor laboratory of the tower and the targets were placed 1.4 km away on the ground. The beam quality of the laser output was measured both near and at 1.4 km distance, and the results confirm a near diffraction-limited beam with $M^2 < 1.3$ over the full wavelength range. Spectroscopy of different targets was also demonstrated at distances of 1.4 km. Due to the small slant angle with respect to the ground, atmospheric turbulence is found to introduce a $\sim 5.8\%$ variation in the beam stability, far greater than that of the laser alone. A SWIR camera was placed adjacent to the laser transmit aperture in the tower laboratory to collect imagery of the backscattered laser radiation from the targets placed on the ground at 1.4 km distance. In addition, the camera was placed adjacent to the laser in the tower, and diffuse reflection of the light off of the ground target was measured in the tower. To our knowledge this was the first ever experiment of two-way propagation of active hyperspectral imaging illumination over a long distance, and it demonstrated the feasibility of the overall concept of using a SWIR-SCL as the broadband illuminator.

5. CHANGE DETECTION BY SYNCING SWIR-SCL AND CAMERA

In the change detection experiment the camera frames with laser off are subtracted from the frames with laser on, thereby cancelling out artifacts associated with the sun illumination, the change in angle of the sun, and shadows. To perform the change detection experiments, the output of the SWIR-SCL was modified so that it could be modulated and synchronized with the frame rate of the SWIR camera (a Sensors Unlimited, Inc., SU640CS InGaAs Camera). Before going into the experimental details, we provide examples of these images at various times of the day at the WPAFB field tests in Fig. 16. During the morning and mid-afternoon, the laser spot was not visible to the eye in the SWIR camera as the solar irradiance dominated the signal, but the difference imagery did show the laser spot. However, in the early evening the solar irradiance was reduced such that the laser and solar irradiance became similar in magnitude and the laser spot became visible.

We also observed that the captured imagery had a larger dynamic range in the evening as the maximum and minimum pixel values indicate because the integration time and gain of the camera was varied throughout the day to avoid saturation of the scenery. The laser spot was also noticeably smaller in the early evening collection due to refocusing that took place at 1600. Fitting of the spot size using a two-dimensional (2D) Gaussian fit indicates that the SWIR band peak irradiance increased from approximately 180 W/m^2 to around 500 W/m^2 after refocusing.

The SWIR-SCL electronics were designed for computer control, and this enabled external modulation of the laser output. In particular, the modulation pattern was imposed on the seed laser, and external modulation could be achieved for modulation frequencies ranging from about 15 Hz to about 5 KHz. High repetition rate (50 MHz) mini-pulses were used during the off-time to maintain gain saturation in the pre- and mid-amplifier stages, yet result in essentially zero output [17]. Laser transients established the maximum modulation frequency during turn-on, and thermal cycling stresses determined the minimum frequency, which could limit the life

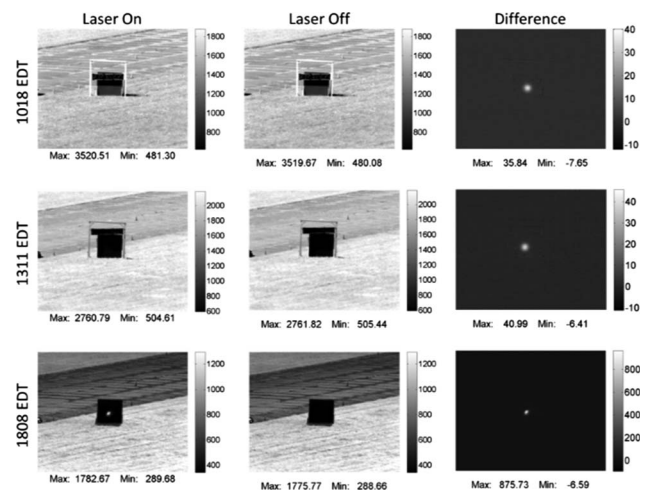


Fig. 16. Examples of change detection images throughout the day at WPAFB.

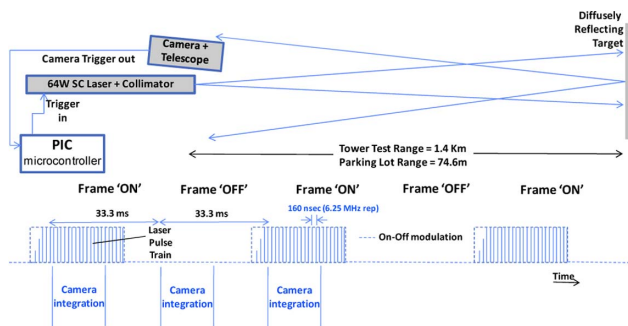


Fig. 17. Schematic and timing diagram for the change detection measurements.

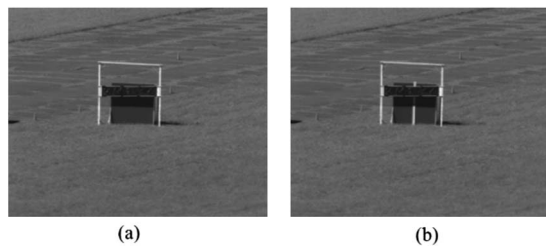


Fig. 18. 8' × 8' target board. (a) Shadow structure; (b) Change detection board.

of the fiber in the power amplifier stage. More details on the modulation technique for the SWIR-SCL are provided in [17]. For the change detection experiments described here, we operated at the lower frequency limit of external modulation. We operated the laser at 15 Hz to achieve alternating laser on/laser off frames for the 30 Hz frame rate of the SWIR camera. As the following results show, we were able to operate the SWIR-SCL at 15 Hz modulation rate without observing any degradation in the laser performance for long periods of time.

For the change detection, the 30 Hz camera trigger output was used to control the laser modulation. Since alternate frames are to be “on” and then “off,” we used a programmable

microcontroller to trigger the laser using every other frame (15 Hz). Figure 17 presents a schematic diagram of the experiment, along with a time diagram showing the laser pulse train during the laser “on” time. As drawn, the camera begins integrating after the laser pulse intensity has stabilized and stops integrating before the pulse train ends. During daylight and laser illumination, the high sensitivity of the SWIR camera requires that the frame-integrated “on” time be significantly shorter than the available 33.3 ms to prevent saturation of the camera’s detector array. Typical integration times were between ~1 and 5 ms.

A. Field Test of Change Detection at 1.4 km Distance

The experimental setup for change detection was the same WPAFB testbed with the SWIR-SCL in the 12-story tower and the 8' × 8' gray-painted target board in the outdoor range at a 1.4 km distance (Fig. 9). Based on measurements over various wavelength ranges, the target board spectral reflectance was determined to be $13\% \pm 1\%$. We integrated a UTC Aerospace GA640CA SWIR band camera with a Celestron CP-6A Newtonian astronomical telescope with a 750 mm focal length $F/5$ primary mirror using a custom-built eyepiece adaptor. We then placed the assembly in front of an open window, which provided a clear line of sight to the targets on the range. We used a laptop with custom designed software to control the camera and collect the captured frames.

For change detection and understanding shadow effects, we also introduced a horizontal strip of board in front of the target board with an adjustable height [Fig. 18(a)]. In particular, an A-frame with an adjustable 2' × 12' opaque structure cast a sun shadow that intersected the irradiated area of the target board. The position of the structure was adjusted to keep the shadow positioned at a constant position on the board until the sun passed behind the plane of the target board. A 5 - 1/2' × 9' unpainted board was placed vertically against the front of the 8' × 8' target for the change detection test [See Fig. 18(b)].

Table 2 shows how test conditions varied throughout the day and how those changes were expected to impact the various tests. By exploiting the full range of test conditions, we anticipated covering from the most stringent to the most forgiving

Table 2. Testing Conditions and Expected Impact on Sensitivities

Time of Day (EDT)	0700–1300	1300–1900	1900–2130	2130 and later
Natural sources of irradiance	Direct solar and indirect sources	Indirect (sun above or behind target)	Sunset through end of Astronomical twilight	Lunar/star light irradiance only
8' × 8' target board (SNR/SCR)	Most demanding SNR/SCR	No direct competition from sun	Rapid decrease in residual ambient lighting conditions	Most favorable to SNR
5.5" wide board no reflector (change detection)	Easy change detection board/no board in ambient	Still easy to detect changes in ambient	Rapidly increasing difficulty to detect change using only ambient	Must have active irradiance
5.5" wide board with 2.125" × 1.625" reflector (change detection)	Can detect board w/wo reflector, but better active	Active better	Rapidly increasing difficulty to detect change using only ambient	Must have active irradiance
Shadow board (ambient lighting immunity)	Good for nulling out changes due to shadows	Not used	Not used	Not used
5" corner cube (ranging tests)	Good contrast against sunlight	Not used	Not used	Good for range testing

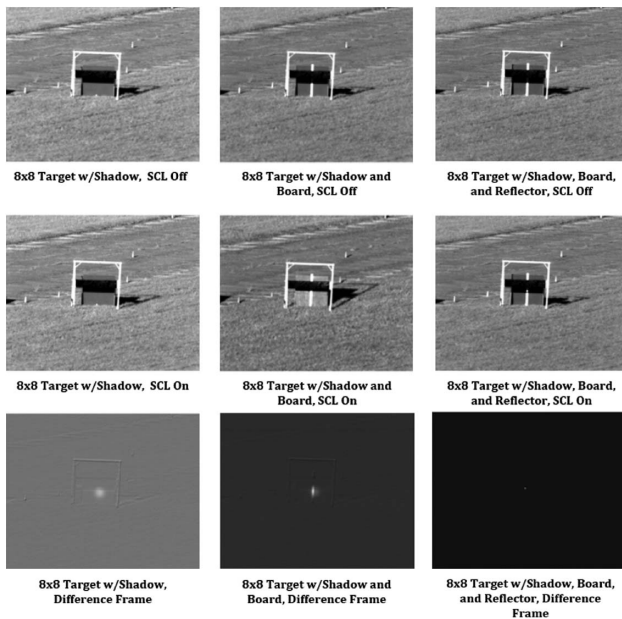


Fig. 19. Examples of change detection frames.

conditions, allowing us to determine the onset of success. Note that SNR refers to signal-to-noise ratio, while SCR refers to signal-to-clutter ratio.

We collected change detection data sets throughout the day with varying solar conditions. During each collection time we collected three data sets. The first was the $8' \times 8'$ target with a shadow crossing the center of the target, Fig. 18(a). Note that the shadow could only be cast across the front of the target before solar noon. Second, we placed the $5 - 1/2'$ board in front of the $8' \times 8'$ target, Fig. 18(b). Third, we turned the board so that a $2 - 1/8' \times 1 - 5/8'$ bicycle reflector was visible to the tower (described further in the range ranging experiments). Figure 19 illustrates examples of the image frames collected with the different target conditions and with the laser on or off. Also shown is the time averaged background subtracted images showing the reflected laser beam. In the case of the bike reflector, the beam profile is hidden because of the very strong return from the bike reflector's retroreflection in comparison to the mostly Lambertian returns of the other objects in the scene.

B. Computation of SNR and SCR for Data Collected

The acquired data per individual collection consisted of 2000 frames collected at 30 Hz frame rate. The laser was irradiating the target board in the scene every other frame. The pairing of adjacent frames with laser on and off created stable difference frames independent of the ambient lighting conditions. Collection of 1000 sequential frames with laser on and then a subsequent collection of 1000 frames with laser off would have been more susceptible to the uncontrolled ambient conditions.

Some definitions and descriptions are worth noting before discussing SNR/SCR analysis. Signal is defined as the contrast difference between the object of interest and its surround. Defining surrounding area is open to interpretation and typically is processing dependent. The second set of definitions

relates to the terms noise and clutter. Based upon the description given for signal above, noise is similarly a spatial phenomenon that tends to obscure or confuse the detection of the signal. Scene-based noise or clutter is due to structure in the scene. This texture can serve to hide weak signals. Camera-based noise is broken into two parts, temporal and pattern noise that is fixed in time. Temporal noise is only noticeable when compared against other frames. Thus, in any single frame analysis scheme, the temporal noise is indistinguishable from the fixed pattern noises. This also holds for quantum effects due to the interactions of the incoming radiation with the detector materials.

SNR and SCR were computed using identical methods, but the difference implies something about the image being analyzed. Clutter is defined as image content that is not part of the signal of interest. Similarly, noise implies that the clutter has in some way been addressed and virtually removed leaving only true signal and accompanying noise sources. For the SWIR band under daylight irradiance, a raw image is expected to be dominated by clutter; whereas in low light levels temporal and spatial noises are expected to dominate. One way to minimize the impact of clutter noise in a daylight image is to capture images both with the laser irradiance present (foreground) and with it absent (background).

Assuming perfect registration between the paired images and that any changes due to ambient conditions are slowly varying in time relative to the frame rate, the difference frame minimizes the impact of scene clutter by cancellation. However, the signal present in the foreground is absent in the temporally adjacent background and, therefore, is virtually untouched in the differencing process. This differencing process also minimizes the impact of fixed pattern noise, which is pixel-to-pixel response differences that are stationary with respect to their pixel address. Noise that remains is due to any temporal noise present in the image due to normal detection processes and those that violate the assumption of spatial registration of the images. In perfectly registered images, normal temporal variance in the difference image is increased by a factor of 2 over the single image temporal variance. However, violations of the perfect registration assumption due to such factors as sensor platform vibration and atmospheric scintillation lead to increased variance at pixels located where steep irradiance gradients occur. As a result, if there are sharp gradients and they are included in the area of interest (AOI) evaluated, the spatial noise estimates of the difference images can be significantly increased.

The SCR and SNR are both computed as

$$\text{SNR or SCR} = \frac{\mu_{\text{core}} - \mu_{\text{sur}}}{\sigma_{\text{sur}}}, \quad (1)$$

where μ_{core} is the average focal plane array in the core region, μ_{sur} is the average focal plane array response in the surround, and σ_{sur} is the standard deviation of the response in the surround region. This equation is applied to any image being analyzed, whether it is a single frame or a difference frame. SCR is reserved for full foreground image computations whereas SNR in this document refers to all difference frame computations and to highly restricted surround foreground computations such as defined as the on-target board surround.

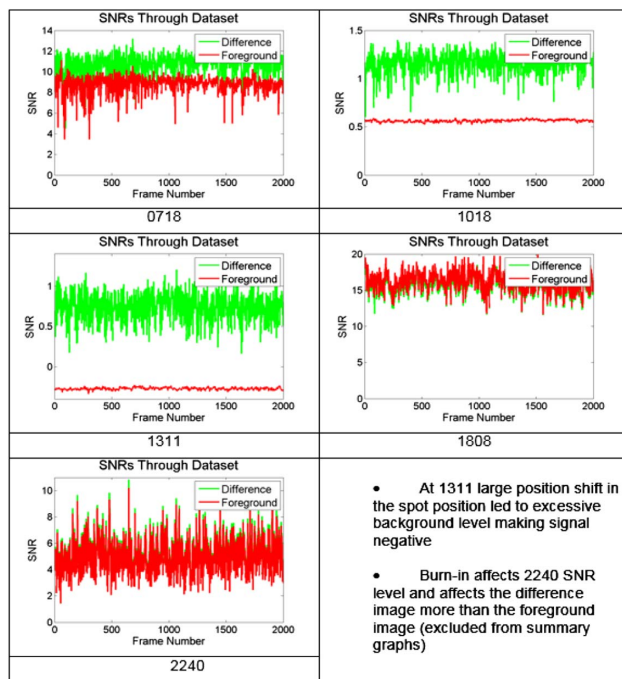


Fig. 20. On-target board SNR temporal plots throughout day (number below corresponds to time of day of measurement).

Figure 20 collects a series of SNR performance comparison plots throughout each of five data sets. Two lines appear on each plot indicating the single frame SNR computed using the on-target board surround described above. The green line represents the difference frame SNR, while the red line indicates the foreground frame only SNR. Performances indicated assume a prior knowledge of the location of the spot and that the irradiated area used in the analysis is a flat Lambertian reflector. Thus, this is the best set of possible conditions to be evaluated. Separation of the data sets within a plot indicates a significant difference in the performance of the two methods. A clear advantage is observable when the sun directly irradiated face of the board. The advantage disappears as the direct irradiance diminishes until it is virtually nonexistent as the sun moves behind the board or the ambient light drops to extremely low levels. Figure 21 recasts and summarizes each of the temporal plots in the form of a histogram.

There are some things to note in this set of plots that confuse the above conclusions. First, morning fog, although relatively benign for the SNR computations, would adversely affect spectral reflectance estimates during hyperspectral imaging sensing because it adds a spectrally dependent return signal to the desired reflectance obtained directly from the board. Second, the negative SNR at 1311 is due to the drift of the beam center causing off target board signals to enter the computation of background level and noise. The increase in the average background is enough to make the difference signal negative and, therefore, invalidates this particular data point for foreground SNR estimation. Third, the variance of the difference frame SNR is considerably higher than that for the foreground only data. This is explained by the introduction of large

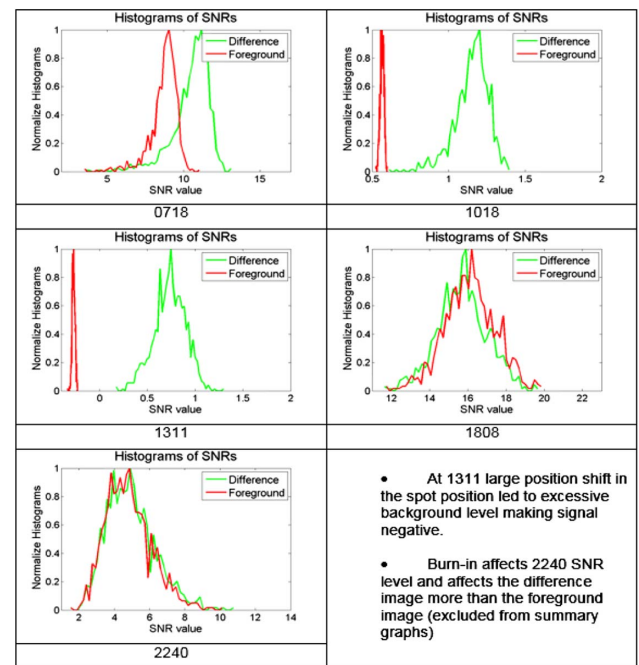


Fig. 21. On-target board SNR histograms throughout day (number below is time).

fluctuations generated by platform jitter and atmospheric scintillation, causing larger swings in the computed noise level and mean signal levels in the surround regions.

The difference image with jitter/turbulence effects becomes a high-pass filter emphasizing edge effects. Small local or global motions mean that edges with fast changes are not eliminated effectively and generate large variations with respect to lower spatial frequency (non edge) areas adversely affecting SNR. Fourth, the performance of the foreground image at 2240 appears to slightly exceed that of the difference frame. This effect is due to the appearance of a negative ghosting or burn-in image effect. Note that the 2240 images, although reported here exhibited anomalous behavior due to the ghosting issue and have purposely been excluded from some of the summary analyses. The summary graphs typically end with the 2140 data collections, after sunset but before the onset of the anomalies.

Correlations between on target board SNRs and ambient conditions are illustrated in the left half of Fig. 22. The hours since midnight EDT on 3 September 2014, in Dayton, Ohio, are noted along the bottom of the graphs. There are four vertical dashed lines denoting local sunrise and sunset (black), local solar noon (left most red line), and the point of SWIR-SC laser optical system readjustment (right most red line). Error bars are included on the data points on the SNR graphs. These indicate the standard deviation of the SNRs computed throughout the test collection. The plots are on a linear rather than a log scale to allow for negative SNRs to be shown with their correct sign. Note that as the solar irradiance increases, the SNR computed decreases as expected. Relative humidity remained high until just after the 0800 series of collections and then began to decrease. It remained low until afternoon when it began a steady climb. However, it never reached the 100% level indicative of

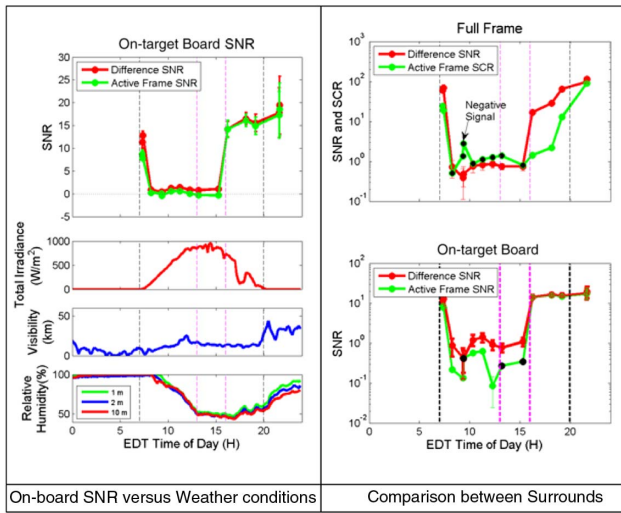


Fig. 22. Summary of SNR and SCR results for field tests.

fog although dew may have collected on objects in the field changing their reflectance characteristics. Lack of evening fog is confirmed by the visibility, which was exceptionally good for the Dayton area from late afternoon into the evening. However, the 2240 data showed anomalous behavior and, therefore, were dropped from the summary analyses.

The right-hand pair of plots in Fig. 22 shows a comparison of the full field surround performance to the on-target board surround performance. Surround is the region of an image surrounding the signal that is used for computation of background and noise/clutter statistics. Vertical markings are defined as before; however, the data is now plotted on a semi-log scale with the absolute value of the SCR or SNR plotted on the logarithmic axis. Negative SNRs and SCRs are marked with black dots instead of green and should be considered as a non detect condition as they are expected to have a positive value for detection. The same general performance shape is present in both sets of data. However, due to the smaller impact that the signal corruption has on after full image dark noise variance, both the noise is lower and the signal is larger leading to the significant difference between the on-target board and full image SNRs. Qualitatively from 0800 until about 1600, the performance of the two techniques is very similar. However, under lower light conditions, the full field calculations give a significant increase in SNR contrast against surround. Note that there are three points in the on-target board foreground SNR that are negative.

Restricting consideration to the full image SNR/SCR curves, there is significant difference throughout the day. The difference frame technique always produces a positive SNR and rises more quickly as the sunsets than does the SCR. The two metrics start to converge after sunset and are indistinguishable by the end of astronomical twilight.

In summary of the change detection experiments, please note that following observations:

1. Performance of full field measurements during high irradiance periods is significantly enhanced using frame differencing as the signal is small compared to the clutter noise.

However, the advantages of frame differencing rapidly diminishes to insignificance as the sunsets.

2. Performance of on-target board SNR performance is similarly enhanced during direct solar irradiance due to a subtle reduction in noise from shadows. This advantage dissipates rapidly when the sun no longer directly irradiates the target board.

3. Performance is strongly linked to the position of the sun relative to the normal of the target board.

4. Signal detection on foreground frames is only possible on benign backgrounds.

5. Signal detection was successful under any conditions for difference imaging and can be improved through frame-to-frame averaging to remove jitter and speckle effects.

6. RANGING AT DISTANCES AROUND 1.4 KM IN FIELDS TESTS

Next, we took advantage of the pulsed nature of the SWIR-SCL output to measure the distance to the target. Since the SWIR-SCL is a pulsed laser, it has the potential to make time-of-flight absolute range measurements and, since the pulses are sub-nanosecond, the range measurements can be quite accurate. Figure 23 shows schematically the measurement concept. The pulse train generated by the 64 W SWIR-SCL is expanded and sent through a collimator to the target scene. The receiver is comprised of a telescope adjacent to the SWIR-SCL, a telescope mount, and a SWIR camera. A REIGL Lasertape FG21 laser range finder (resolution of ~1 m) was also integrated, to act as a range truth measurement, onto the same tripod mounting plate as the SWIR camera and telescope. Figure 24 includes a photograph of the camera, telescope, and range finder.

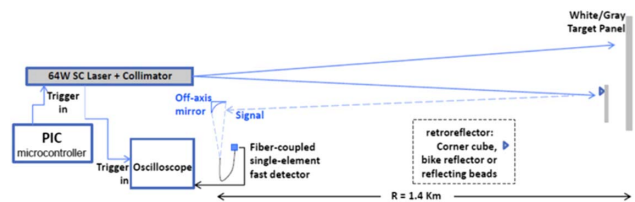


Fig. 23. Basic experimental configuration for laser ranging.



Fig. 24. Photograph of the camera, telescope, and range finder for laser ranging.

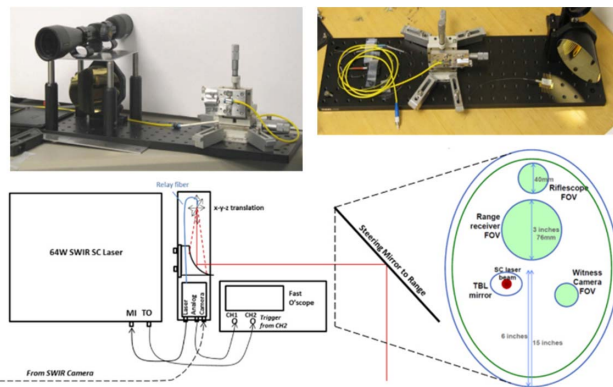


Fig. 25. Range detector diagrams showing the detector and steering mirror space budget.

For the basic experiments, this scene consisted of an $8' \times 8'$ target board where the change detect experiments took place. For the ranging experiments, four different retroreflectors were used during the experiment: a $2 - 1/8'' \times 1 - 5/8''$ single bicycle reflector; a $2' \times 2'$ square filled with red rectangular bicycle reflectors; a $1''$ corner cube; and a $5''$ corner cube. The single bicycle reflector was attached to the center of the board that was placed in front of the $8' \times 8'$ Target (cf., Fig. 18). The $2' \times 2'$ bicycle reflector square, the $1''$ corner cube, and the $5''$ corner cube were all used for range detection testing; however, only the $5''$ corner cube returned sufficient signals for the range sensor to detect consistently. Range measurement points were pre-surveyed at 1400, 1401, 1402, 1404, 1408, 1416, 1432, 1464, and 1528 m slant ranges from the 12th floor of the tower. During the range test, the $5''$ corner cube was moved to one of the pre-surveyed locations and measurements were taken.

We designed a range-receiver to measure the last pulse received in a pulse train. A 3-inch diameter 9-inch focal length gold-coated off-axis parabolic mirror gathered return radiation from the target and focused it onto a fiber-coupled ($9 \mu\text{m}$ core) fast $75 \mu\text{m}$ diameter InGaAs PIN photodiode (PD-LD Inc., Pennington, New Jersey). A 160 mW 1490 nm laser diode with fiber pigtail was spliced to a 50:50 beam combiner along with the receiver fiber to serve as a back-propagating bore-sighted alignment laser.

The time-of-flight was measured by accurately determining the time between the last pulse leaving the laser and its arrival at the range-receiver's off-axis parabolic mirror. The laser provides a trigger output signal, which precisely indicates when the last pulse is generated. To allow the last pulse in an on-frame pulse train to be distinguished from the others arriving at the receiver, a delay was added between the last full power pulse and the first mini-pulse. This delay is 120 ns longer than the typical time between pulses while the laser is on (i.e., the pulse repetition time), providing a clear signature indicating the last pulse. This signature allows for automated as well as manual detection of the last pulse in an on-frame.

Figure 25 illustrates the range detector as well as a diagram depicting the arrangement on the optical table during the tower test. Major ranging sensor components are the fiber optics with $x - y - z$ positioner that acts as the collecting optics in

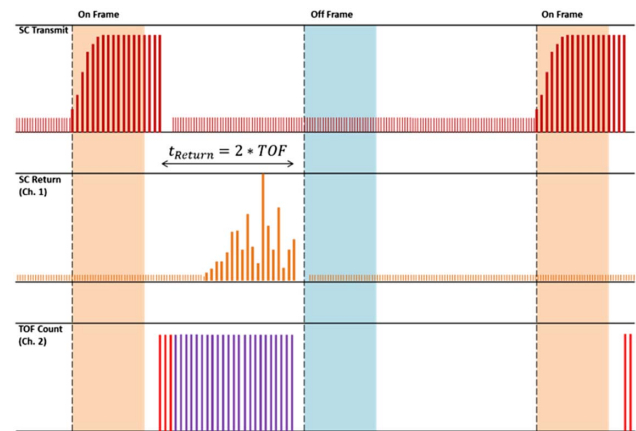


Fig. 26. Schematic of timing diagram to compare the measured oscilloscope signals.

conjunction with the focusing mirror, the ranging sensor with circuitry including the PIC microcontroller and the InGaAs PIN photodiode and its amplifiers, denoted as the laser analog camera, the rifle scope for aligning, and the steering mirror that directs the beam to target and the received signal to the sensor. Other equipment involved in the ranging measurements includes the SWIR-SCL and the 500 MHz oscilloscope. The driving scheme for the change detect synchronization between the SWIR camera and laser are as follows: (1) the camera provides the trigger signal to the PIC, (2) the PIC selects every other frame to trigger the laser and provides the timing delays for change detection, (3) the laser output control signal from the PIC is connected to the modulation input (MI) of the laser, (4) the trigger output (TO) from the laser goes to the oscilloscope (Ch. 2) for triggering and time-of-flight determination, and (5) the received photodiode pulses are amplified and output to the oscilloscope (Ch. 1). Figure 25 also shows the received signal optical path (red line) as received from the steering mirror and the space budget of the steering mirror.

The data acquisition and measurements result from comparing the transmitted and received optical signals as shown in Fig. 26. This figure shows the general method used to measure the time of flight. The camera integration times (shaded regions) repeat at the 30 Hz frame rate. The top row shows the waveform representing the transmitted SCL pulse train, which turns on during every other frame's integration time. The middle waveform represents the received optical signal (Ch. 1) that is delayed by approximately twice the time of flight (TOF) to the target (t_{Return}). The bottom waveform represents the output from the laser's Trigger Output (TO) (Ch. 2 in Fig. 25). The measured time of flight was determined experimentally by comparing the beginning of the pulse time count (red pulses in Ch. 2) to the final pulse of the received signal (Ch. 1). This could be offset from the true time of flight due to electronic delays and, therefore, must first be calibrated with a known standard. This study used the commercially available range finder with 1 m resolution.

The TO signal, as shown in Fig. 26, has a few fixed pulses that were always visible in the oscilloscope signal and a variable pulse train length that was determined by the final edge of the

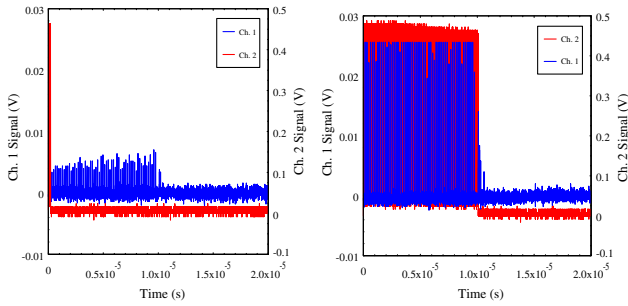


Fig. 27. Example measured oscilloscope signals (Range = 1408 m).

received optical signal, assuming the signal was strong enough to trigger the internal circuitry of the PIC. The utility of this variable pulse train is that the spacing between these pulses is the internal clock time (100 MHz), so that later improvements could allow for digital counting of these pulses to determine the time of flight with a 1.5 m resolution. Unfortunately, during the tower tests, we found that receiving consistent return signals above the required threshold to trigger this counting pulse train was hard to obtain, indicating that future improvements of the detector should incorporate some additional signal amplification to ensure proper operation of the ranging sensor as intended. Figure 27 shows example waveforms that were taken during the tower test. Both plots compare the TO signal (red) to the received optical signal (blue) for the same range (1408 m). The difference between these two plots is the magnitude of the return signal. The weaker signal (left) did not meet the TO threshold, while the stronger signal (right) did. This resulted in an inconsistent TO pulse train width. These inconsistencies lead to the need to manually measure the time of flight by analyzing the oscilloscope waveforms. The manual method was implemented for all ranging analysis reported herein.

Experimental Results for Laser Ranging Measurements in Field Tests

Figure 28 shows comparisons between the pulse waveforms measured using the corner cube at different ranges. This figure shows a zoomed out (left) and zoomed in (right) waveform.

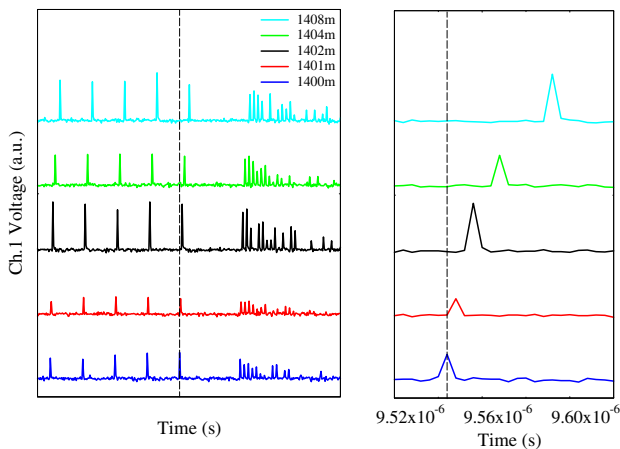


Fig. 28. Range return pulse comparisons.

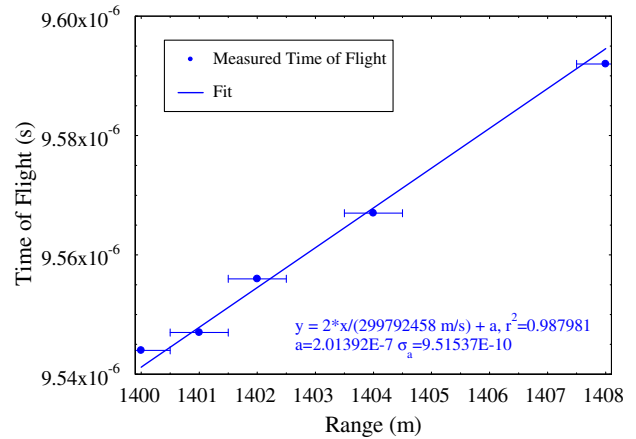


Fig. 29. Measured time of flight with fit.

The end of the laser pulse train was identified by a gap in the pulse train followed by an exponentially decaying higher frequency pulse train. By comparing the shifts in positions of the last pulse of the received laser signal at different ranges, we calculated the resolution of the ranging sensor. It is worth noting that the pulse-to-pulse variability shown in Figs. 27 and 28 is probably due to sampling artifacts for the very narrow laser pulses.

Figure 29 shows the measured time of flight versus truth range distance. Comparing these results to the theoretical fit, and using the formula

$$TOF = \frac{2 \times Range}{c} + t_{offset} \tag{2}$$

gives a $t_{Offset} = 201.4$ ns. The error bars in the range direction reflect the certainty of the truth range finder that was used to calibrate the slant range distances. The sensitivity of the range measurements were tested experimentally by taking several waveforms using the oscilloscope and measuring the time of the last pulses maximum value. Figure 30 summarizes the

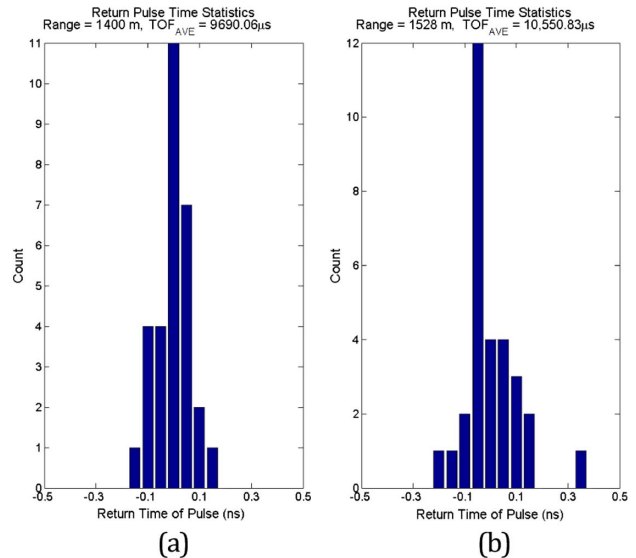


Fig. 30. Histograms of return time of the final pulses for range targets at (a) 1400 m and (b) 1528 m.

results in its histograms. These results suggested that the sensitivity of the manual method was accurate to within 0.1 ns (~ 1.5 cm range resolution), much less than the 1 m resolution of the range finder.

7. DISCUSSION: ANALYSIS OF CHANGE DETECTION DATA

A metric to quantify the changes of placing an additional object in the target area was the adaptation of the Pearson's correlation coefficient. The correlation coefficient gives a single value to quantify how related one random variable is to another. The modified correlation coefficient used in this paper is calculated as

$$M_{1\text{Cross}}(t) = \frac{\sum_{i=1}^I \sum_{j=1}^J (X_{i,j}(n) - E[\bar{X}_{i,j}]) \sum_{i=1}^I \sum_{j=1}^J (Y_{i,j}(n) - \alpha E[\bar{X}_{i,j}])}{\sqrt{\sum_{i=1}^I \sum_{j=1}^J (X_{i,j}(n) - E[\bar{X}_{i,j}])^2 \sum_{i=1}^I \sum_{j=1}^J (Y_{i,j}(n) - \alpha E[\bar{X}_{i,j}])^2}}, \quad (3)$$

where $\mathbf{X}_{i,j}(n)$ and $\mathbf{Y}_{i,j}(n)$ represent the two difference frames regions of interest (ROI) from two different sets of data. The frame pixel location is given as i, j and the frame is designated as n . Finally the temporally averaged difference frames are designated with $\bar{\mathbf{X}}_{i,j}$ and $\bar{\mathbf{Y}}_{i,j}$. In this paper, the two sets of data are the collections with, \mathbf{Y} , and without, \mathbf{X} , the board in scene. Figure 31 shows a sample non-differenced frame with and without the board from the noon data collection. The ROI used for the calculations is outlined in red.

The adaptation used to tabulate the results in this paper treats $\bar{\mathbf{X}}_{i,j}$ as a template. The main focus is to see how much data with the board in scene varies from this template. To do this on a difference frame basis, the variations between $\mathbf{X}_{i,j}(n)$ and $\bar{\mathbf{X}}_{i,j}$ must still be included in the calculation. This ensures the effects of temporal variation in the difference frames where there is no board still has an impact on the result.

The final equation to calculate the correlation coefficient is

$$\alpha = \frac{\sigma_Y}{\sigma_X}. \quad (4)$$

The standard deviation calculation for both σ_X and σ_Y are spatial calculations after a temporal mean on board and no board with the laser off. An issue arises when the standard

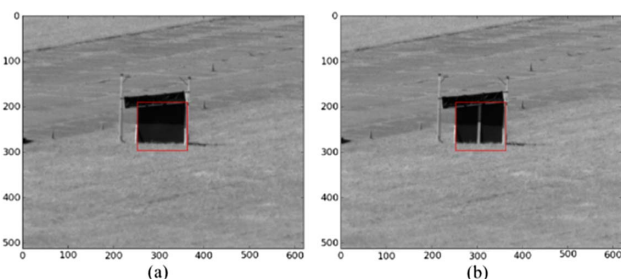


Fig. 31. Sample of non-differenced frame (a) without board and (b) with board.

deviation is calculated over the whole frame due to the fact the presence of the board affects the global standard deviation of the image. Therefore, the standard deviations were calculated on subsets on the image. In Fig. 32, the area highlighted in red was excluded from the temporally averaged differenced frames spatial standard deviation calculation. The number of data points outside of the red region still provides enough of a sampling to estimate a proper standard deviation.

The α ensures the balance between the two data sets due to different integration times and gains that were used to remove saturated pixels from the imagery. This is important as each data set has a unique integration time and camera gain. The gain affects the number of electrons necessary to generate a digital count. The integration time affects the SNR. Another result

of varying the integration time was the change in the duty cycle of the laser. A smaller integration time would lead to a shorter duty cycle on the laser output. Here we assume that there is a linear relation between the integration time and duty cycle. The alpha parameter then scales not only the scene light levels but also the laser light levels appropriately to match between the data set of no board and board in scene. Another variable that has been taken into consideration is the time between board/no board collections for any given time of day.

Figure 33 shows a plot showing the coefficients calculated by using the equation for $M_{1\text{Cross}}(t)$ for the 0722/0742 no board/board collection. The mean for all the data points is calculated along with the standard deviation. The calculations performed on 0722/0742 collections were also calculated on the data sets outlined in Table 3.

An error bar plot was then generated to show the fluctuations in all the time of day collections as plotted in Fig. 34. The further the coefficient is from 1, the easier it is to distinguish the change of placing the board in the scene.

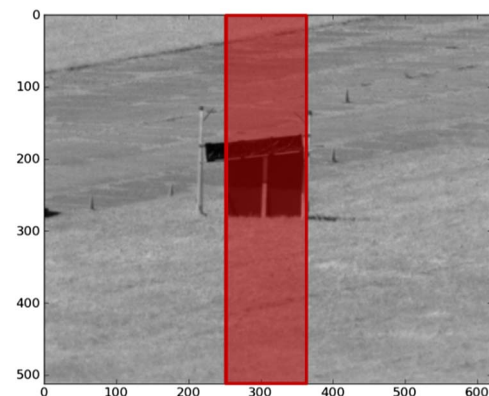


Fig. 32. Windowed portion for standard deviation calculation.

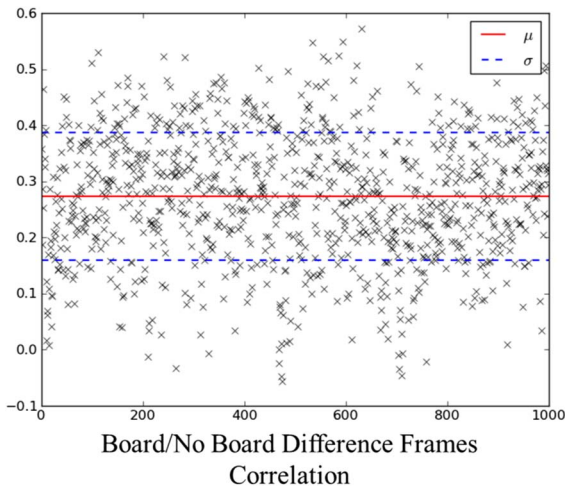


Fig. 33. Sample correlation through data set.

Table 3. All Time-of-Day Datasets Used in Calculations

Time of Day [No Board, Board]	Difference (minutes)
[0722, 0742]	20
[0814, 0818]	4
[0921, 0925]	4
[1018, 1021]	3
[1115, 1122]	7
[1216, 1241]	25
[1311, 1314]	3
[1517, 1521]	4
[1616, 1620]	4
[1808, 1815]	7
[1909, 1914]	5

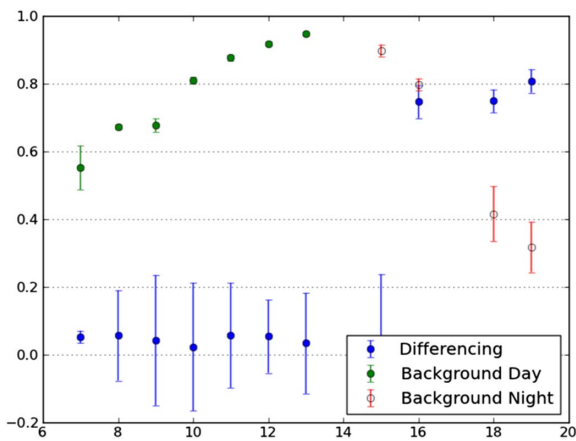


Fig. 34. Correlation throughout day.

Figure 34 shows the mean and standard deviations of the Pearson correlation coefficients described above within the ROI described in Fig. 31. In one case, we calculated the correlation coefficients using only the background (laser off) imagery, labeled as “Background Day.” As expected during the daytime, the correlations become closer to one as the

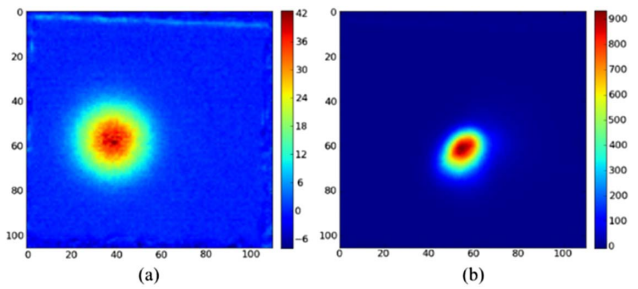


Fig. 35. Temporally averaged difference frames. (a) 1500 and (b) 1600.

sunlight transitions from front irradiating to back irradiating the target board. Unexpected, however, is the response that occurred in the late evening where this correlation began to decrease once again. This behavior has been plotted with a different color and labeled as “Background Night” to distinguish it from the expected behavior that occurred in the Daytime.

The reason for this unexpected behavior may relate to the unexpected image burn-in effect discussed earlier. This resulted in the laser off frames from not being completely independent of the laser spot and, therefore, still able to detect the presence of the board. Most importantly, this figure is the correlation coefficients obtained from the difference frames, which were found to be very close to zero and stable throughout most of the daytime and afternoon. The only jump in sensitivity occurs after the beam refocusing that resulted in a smaller portion of the board being irradiated by the beam than earlier in the morning, but again this result is fairly stable during the late afternoon/evening collections.

Figure 35 illustrates the differences in the beam shape and the drift throughout the collections is illustrated. These results suggests two things: (1) the difference frame processing significantly improves the uncorrelated nature of the change detect processing when compared to the background frames only, and (2) the difference frame correlation coefficients are significantly more stable than the background frames and seem most sensitive to the properties of the laser rather than the ambient irradiance conditions.

Another aspect of the change detect processing that should be mentioned is the corresponding time of the collections used and the time difference between the no board/board data collections throughout the day. Table 3 outlines the difference in time. On average, the difference between the board/no board collection was 8.08 min. The larger differences in time can be contributed to redoing collections due to saturations on the camera sensor. The 0700 collection had the retroreflector data set captured first before just the board data capture. Another delay was the laser shutting down affecting the 1200 collection. It is import to note there is no correlation with the difference time and the standard deviation of the correlation coefficients for a given set.

Simulated SNR Performance Compared with Measurements

A theoretical computation of the expected SNR was computed using an atmospheric model called the Laser Environmental

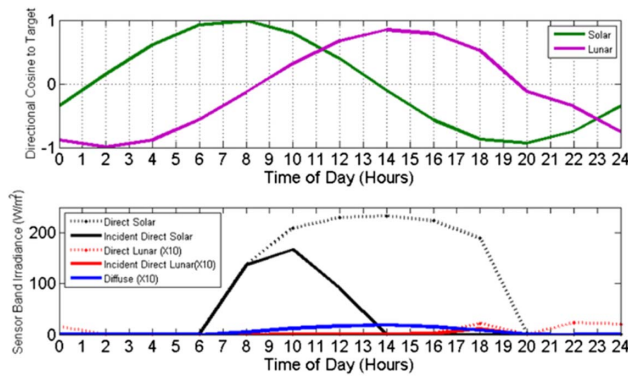


Fig. 36. Predicted ambient irradiance conditions during test.

Effects Definition and Reference developed by the Center for Directed Energy at the Air Force Institute of Technology. This software provides capabilities to model spectral radiance caused by direct and diffuse sources of irradiance from the sun or moon. In particular, the positions of the sun/moon at WPAFB at the time of the collection could be modeled. Using this model, ambient irradiance conditions were predicted on the target board every two hours throughout the 24-hour testing period. The predicted irradiance included direct solar, direct lunar, and scattered skylight irradiances on the target. Only primary irradiance was considered, ignoring reflectance generated radiance sources due to nearby objects. Also, the effects of clouds were not calculated, although the phase of the moon was calculated. The effective irradiances were integrated over the hemisphere determined by the plane of the target board and weighted by the spectral response of the sensor system. Figure 36 collects the pertinent elements of the model.

The signal was estimated based upon the expected irradiance due to a best fit circularly symmetric 2D Gaussian beam profile to pre- and post-1600 realignment and weighted by the expected in-band radiance profile of the laser. Since both the laser and the signal were observed within the confines of the target board, specific reflectance profiles were assumed to be flat and equal for both the laser and the solar radiance sets. We assume that the background noise could be calculated from the irradiance on the board based on Poisson statistics. Noise was estimated using a combination of background limited performance based upon photon arrival statistics (Poisson statistics) and an adjustable fixed equivalent noise (effective sensor noise) used only to tune the overall predicted SNR to a qualitatively comparable range. The equation used to calculate the modeled SNR is

$$\text{SNR} = \frac{[S_{\text{beam}}]_{\text{AVE}}}{\sqrt{S_{\text{direct}} + S_{\text{indirect}} + N_{\text{sensor}}}}, \quad (5)$$

where $[S_{\text{beam}}]_{\text{AVE}}$ is the average modeled detected signal over the beam ROI, S_{direct} and S_{indirect} are the direct and indirect signals from the sun, moon, and solar-scattered spectral within the sensor band, and N_{sensor} is the effective sensor noise. The square root denotes the Poisson statistical nature of the noise expected from the ambient light sources.

The top of Fig. 37 shows the results of the model tuned to approximate the response observed during the test by only

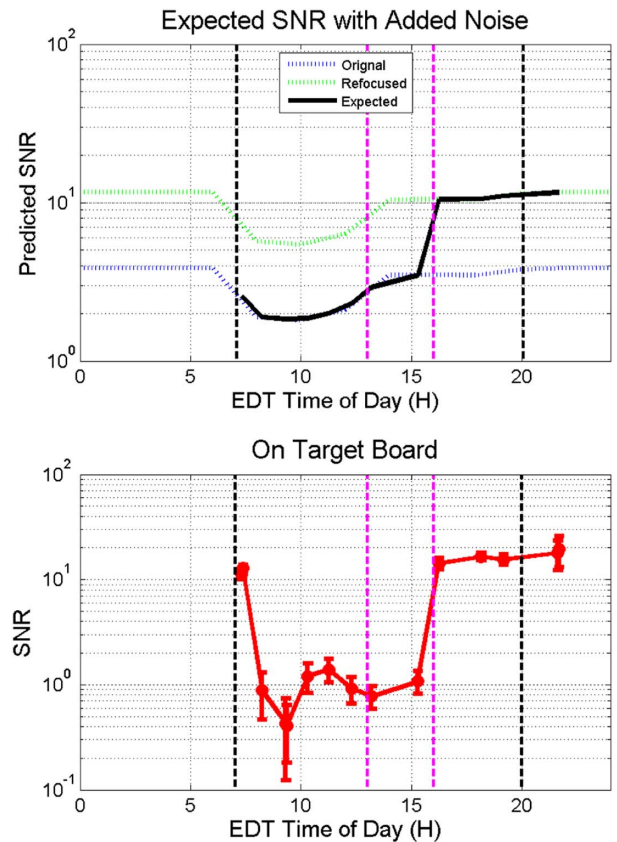


Fig. 37. Comparison between simulated and measured SNR.

adjusting the fixed background level. The black line on this plot was generated using linear interpolation to match correct time sampling times and pre/post SWIR-SC laser optics realignment. The key features to note are the low SNR during the morning hours during maximum direct solar exposure with improving SNR as the sun moves away from target board normal to a maximum after the sun has set. To improve upon this model, a much closer characterization of the camera system would be required along with better control and knowledge regarding the beam profile throughout the day. Additional “at target” board instrumentation to measure irradiance profiles would further aid in the evaluation.

The bottom of Fig. 37 compares the simulated SNR performance with the on-target board SNR performance measured throughout the day (Fig. 22). Qualitatively the curve shapes are very similar except for the early morning test point. It is believed that the amount of direct solar irradiance at this time was reduced due to the early morning fog and the laser backscatter off the fog droplets led to an artificially high return difference signal, therefore leading to a higher than expected signal to noise. The lower SNR ratios in the morning period compared to the predicted could be a result of the sampling errors caused by a reduced beam dynamic range. The measured peak around 1200 EDT correlates well with a peak in visibility that happened around the same period. Under these optimum conditions, there is a reasonable agreement between the measured and predicted SNR.

8. SUMMARY

In summary, we used a SWIR-SCL in field tests at WPAFB to investigate the use of SCL technology to provide active illumination for SWIR hyperspectral sensors to extend their operational window into the night and heavy overcast periods. The SWIR-SCL prototype output 64 W over the continuous wavelength range from 1064 to >1800 nm with a wall-plug efficiency of 15.7%, a beam quality that is nearly diffraction-limited with $M^2 < 1.3$ over the wavelength range, and output variability or fluctuations of $\pm 0.2\%$. The SWIR-SCL is an all-fiber integrated, no moving parts laser that leverages mature fiber optics and telecommunications technologies. The MOPA configuration exploiting the modulational instability mechanism is a simple, cost-effective design and a platform for SC generation over the visible, SWIR, and even mid-wave infrared.

In the field tests at WPAFB, the SWIR-SCL was placed in a 12-story tower, and the beam was directed to targets that were placed on an 8' \times 8' board on the ground at a distance of 1.4 km or more. The beam quality was measured with a SWIR camera, and the laser beam propagated a distance of 1.4 km with the end diameter of ~ 0.9 m. Also, radiometric analysis was performed of different target materials including Tyvek, plywood, blue tarp, and black and gray cloth, and the SNR was estimated for the different materials over the spectral range. In addition, a SWIR camera was placed adjacent to the laser in the tower to measure the diffused reflectance signal from targets placed 1.4 km away. To our knowledge, this was the first experiment of two-way propagation of active hyperspectral imaging illumination over a long distance, and it confirmed the feasibility of the overall concept of using a SWIR-SCL as the broadband illuminator. The 64 W SWIR-SCL has the capability to provide near sunlight-equivalent illumination over multiple square meters.

Using the SWIR-SCL as an active illuminator for HSI can lead to additional benefits beyond extending the operational hours. Since we can control the light source, modulate the output, and synchronize the light source to a SWIR camera, the SWIR-SCL also enables change detection. In change detection camera frames with the laser off are subtracted from the frames with the laser on, thereby permitting cancellation of at least some of the artifacts associated with the sun illumination, the change in angle of the sun, and shadows. Change detection was performed in the field tests with measurements at a distance of 1.4 km using a board and reflector placed in front of the target at different times throughout the day (from early morning dawn through nighttime). The experiments demonstrate that using the SWIR-SCL during daytime and performing image differencing holds potential for reducing some of the uncertainties involved in HSI data reduction due to unknown environmental irradiance. Our tests verify that it is possible to compete with direct solar irradiance and retrieve the reflected signal using difference imaging.

Moreover, by taking advantage of the pulsed nature of the SWIR-SCL, time-of-flight measurements were used to calculate the distance to the target. In our experiments, due to limitations from the collection optics and sensitivity of the receiver, the field tests used the return signal from a 5-inch corner cube

placed on the ground at distances of 1.4 km or more. The experimental results suggest that the resolution of our method was on the order of ~ 1.5 cm even over the 1.4 km distances. Thus, the SWIR-SCL has the potential to serve as an active illuminator for hyperspectral imaging, with brightness comparable to the sun in the SWIR, and an HSI system using this laser could include enhancements not possible simply using sun illumination, such as change detection and laser ranging.

Funding. Air Force Research Laboratory (AFRL) (FA8650-12-D-1344).

REFERENCES

1. M. N. Islam, "All-fiber designs extend supercontinuum sources into the mid-IR region," *Laser Focus World* **13**, 56–60 (2012).
2. B. Johnson, R. M. Joseph, M. L. Nischan, A. Newbury, J. P. Kerekes, H. Barclay, B. Willard, and J. J. Zayhowski, "A compact, active hyperspectral imaging system for the detection of concealed targets," *Proc. SPIE* **3710**, 144–153 (1999).
3. M. L. Nischan, R. M. Joseph, J. C. Libby, and J. P. Kerekes, "Active spectral imaging," *Lincoln Lab. J.* **4**, 131–144 (2003).
4. M. A. Powers and C. C. Davis, "Spectral LADAR: active range-resolved three-dimensional imaging spectroscopy," *Appl. Opt.* **51**, 1468–1478 (2012).
5. V. V. Alexander, Z. Shi, M. N. Islam, K. Ke, M. J. Freeman, A. Ifarraguerri, J. Meola, A. Absi, J. Leonard, J. Zadnik, A. S. Szalkowski, and G. J. Boer, "Power scalable >25 W supercontinuum laser from 2 to 2.5 μm with near-diffraction limited beam and low output variability," *Opt. Lett.* **38**, 2292–2294 (2013).
6. V. V. Alexander, Z. Shi, M. N. Islam, K. Ke, G. Kalinchenko, M. J. Freeman, A. Ifarraguerri, J. Meola, A. Absi, J. Leonard, J. Zadnik, A. S. Szalkowski, and G. J. Boer, "Field trial of active remote sensing using a high-power short-wave infrared supercontinuum laser," *Appl. Opt.* **52**, 6813–6823 (2013).
7. V. V. Alexander, O. P. Kulkarni, M. Kumar, C. Xia, M. N. Islam, F. L. Terry, Jr., M. J. Welsh, K. Ke, M. J. Freeman, M. Neelakandan, and A. Chan, "Modulation instability initiated high power all-fiber supercontinuum lasers and their applications," *Opt. Fiber Technol.* **18**, 349–374 (2012).
8. C. Xia, M. Kumar, O. P. Kulkarni, M. N. Islam, F. L. Terry, M. J. Freeman, M. Poulain, and G. Mazé, "Mid-infrared supercontinuum generation to 4.5 μm in ZBLAN fluoride fibers by nanosecond diode pumping," *Opt. Lett.* **31**, 2553–2555 (2006).
9. C. Xia, M. Kumar, M. Y. Cheng, O. P. Kulkarni, M. N. Islam, A. Galvanauskas, F. L. Terry, Jr., M. J. Freeman, D. A. Nolan, and W. A. Wood, "Supercontinuum generation in silica fibers by amplified nanosecond laser diode pulses," *IEEE J. Sel. Top. Quantum Electron.* **13**, 789–797 (2007).
10. C. Xia, M. Kumar, M.-Y. Cheng, R. S. Hegde, M. N. Islam, A. Galvanauskas, J. F. L. Terry, M. Poulain, and G. Maze, "Power scalable mid-infrared supercontinuum generation in ZBLAN fluoride fibers with up to 1.3 W time-averaged power," *Opt. Express* **15**, 865–871 (2007).
11. J. W. Nicholson, A. D. Yablon, P. S. Westbrook, K. S. Feder, and M. F. Yan, "High power, single mode, all-fiber source of femtosecond pulses at 1550 nm and its use in supercontinuum generation," *Opt. Express* **12**, 3025–3044 (2004).
12. S. Moon and D. Y. Kim, "Generation of octave-spanning supercontinuum with 1550 nm amplified diode-laser pulses and a dispersion-shifted fiber," *Opt. Express* **14**, 270–278 (2006).
13. A. K. Abeeluck and C. Headly, "Continuous-wave pumping in the anomalous- and normal-dispersion regimes of nonlinear fibers for supercontinuum generation," *Opt. Lett.* **30**, 61–63 (2005).
14. B. A. Cumberland, J. C. Travers, S. V. Popov, and J. R. Taylor, "29 W high power CW supercontinuum source," *Opt. Express* **16**, 5954–5962 (2008).
15. K. K. Chen, S. Alam, J. H. V. Price, J. R. Hayes, D. Lin, A. Malinowski, C. Codemard, D. Ghosh, M. Pal, S. K. Bhadra, and D. J. Richardson,

- “Picosecond fiber MOPA pumped supercontinuum source with 39 W output power,” *Opt. Express* **18**, 5426–5432 (2010).
16. O. P. Kulkarni, C. Xia, D. J. Lee, M. Kumar, A. Kuditcher, M. N. Islam, J. F. L. Terry, M. J. Freeman, B. G. Aitken, S. C. Currie, J. E. McCarthy, M. L. Powley, and D. A. Nolan, “Third order cascaded Raman wavelength shifting in chalcogenide fibers and determination of Raman gain coefficient,” *Opt. Express* **14**, 7924–7930 (2006).
 17. C. Xia, Z. Xu, M. N. Islam, J. F. L. Terry, M. J. Freeman, A. Zakel, and J. Mauricio, “10.5 W time-averaged power mid-IR supercontinuum generation extending beyond 4 μm with direct pulse pattern modulation,” *IEEE J. Sel. Top. Quantum Electron.* **15**, 422–434 (2009).
 18. A. I. Ifarraguerri, M. N. Islam, L. Peterson, K. Ke, M. Freeman, J. Meola, A. Absi, and J. Leonard, “A broadband laser illuminator for active hyperspectral imaging,” in *Unclassified Paper in Proceedings of the Military Sensing and Security Conference (2014)*, p. 7.
 19. J. Meola, A. Absi, M. N. Islam, L. Peterson, K. Ke, M. L. Freeman, and A. Ifarraguerri, “Tower testing of a 64 W shortwave infrared supercontinuum laser for use as a hyperspectral imaging illuminator,” *Proc. SPIE* **9088**, 90881A (2014).
 20. J. E. Conel, R. O. Green, G. Vane, C. J. Bruegge, and R. E. Alley, “AIS-2 radiometry and a comparison of methods for the recovery of ground reflectance,” in *Proceedings of the 3rd Airborne Imaging Spectrometer Data Analysis Workshop*, Pasadena, CA, 1987, pp. 18–47.